

A Robust 5G Terrestrial Positioning System with Sensor Fusion in GNSS-denied Scenarios

Hamed Talebian, Nazrul Mohamed Nazeer, Darius Chmieliauskas, Jakub Nikonorowicz, *Senior Member, IEEE*, Mehdi Haghshenas, Łukasz Matuszewski, Mairo Leier, and Aamir Mahmood, *Senior Member, IEEE*

Abstract—This paper presents a terrestrial localization system based on 5G infrastructure as a viable alternative to GNSS, particularly in scenarios where GNSS signals are obstructed or unavailable. It discusses network planning aimed at enabling positioning as a primary service, in contrast to the traditional focus on communication services in terrestrial networks. Building on a network infrastructure optimized for positioning, the paper proposes a system that leverages carrier phase (CP) ranging in combination with trilateration to localize the user within the network when at least three base stations (BSs) provide line-of-sight (LOS) conditions. Achieving accurate CP-based positioning requires addressing three key challenges: integer ambiguity resolution, LOS/NLOS link identification, and localization under obstructed LOS conditions. To this end, the system employs a multi-carrier CP approach, which eliminates the need for explicit integer ambiguity estimation. Additionally, a deep learning model is developed to identify NLOS links and exclude them from the trilateration process. In cases where LOS is obstructed and CP ranging becomes unreliable, the system incorporates an error-state extended Kalman filter to fuse complementary data from other sensors, such as inertial measurement units (IMUs) and cameras. This hybrid approach enables robust tracking of moving users across diverse channel conditions. The performance of the proposed terrestrial positioning system is evaluated using the real-world KITTI dataset, featuring a moving vehicle in an urban environment. Simulation results show that the system can achieve a positioning error of less than 5 meters in the KITTI urban scenario—comparable to that of public commercial GNSS services—highlighting its potential as a resilient and accurate solution for GNSS-denied environments.

Index Terms—Carrier phase positioning, LOS/NLOS identification, Error-state Extended Kalman Filter, visual odometry, 5G terrestrial positioning, sensor fusion.

I. INTRODUCTION

Traditionally, the global navigation satellite system (GNSS) has been the primary technology used for positioning and navigation. It has reliably supported numerous applications for decades. However, recent events have exposed a critical vulnerability in GNSS-dependent systems. In particular, over large geographical areas, GNSS signals have been deliberately disrupted or denied through the emission of strong radio frequency noise, effectively rendering GNSS-based positioning

This work was supported in part by the Swedish Institute through the SafeWork project (grant number 00237/2023), and in part by the EU Interreg Aurora Project ENSURE-6G.

H. Talebian, N.M. Nazeer, and D. Chmieliauskas contributed equally.

H. Talebian, M. Haghshenas, and A. Mahmood are with the Department of Computer and Electrical Engineering, Mid Sweden University, 851 70, Sundsvall, Sweden (email: firstname.lastname@miun.se)

N.M. Nazeer and M. Leier are with the Department of Computer Systems, Tallinn University of Technology, Estonia

D. Chmieliauskas is with the Department of Computer Science and Communication Technologies, Vilnius Gediminas Technical University, Lithuania

J. Nikonorowicz and Ł. Matuszewski are with the Faculty of Computing and Telecommunications, Poznań University of Technology, 60-995 Poznań, Poland (email: firstname.lastname@put.poznan.pl)

inoperable [1]–[3]. Such disruptions highlight the urgent need for a more resilient and robust positioning system—one that does not rely exclusively on a single source of information.

Cellular networks are increasingly being recognized as a promising infrastructure for providing localization services, offering a potential alternative/complementary to GNSS, especially in urban or indoor environments where GNSS signals may be obstructed or degraded. Historically, various positioning techniques have been explored within cellular systems to enable location estimation such as received signal strength (RSS), time of arrival (TOA), time difference of arrival (TDOA), angle of arrival (AOA), angle of departure (AOD), cell ID, and fingerprinting [4].

With the recent widespread deployment of 5G networks several studies have been conducted to analyze the performance of different positioning schemes utilizing 5G networks [5]–[12]. For instance, in [5], primary synchronization signal (PSS) and secondary synchronization signal (SSS) in 5G is utilized to obtain TDOA, enabling user positioning. Similarly, [6] focuses on estimating TDOA using dedicated positioning reference signals (PRS) to improve localization accuracy. In [7], authors estimate TOA and AOA using uplink reference signal and fuse them together to achieve an accurate position estimate. In the same study, an Extended Kalman Filter (EKF) is employed to combine estimation from multiple BSs and improve localization performance. However, all these traditional geometric approaches rely on the assumption of a dominant line-of-sight (LOS) path — an assumption that may fail in real-world conditions. Their performance deteriorates significantly in rich multipath environments or under non-line-of-sight (NLOS) conditions [13]. To address these challenges, researchers in [10]–[12] have explored fingerprinting and machine learning (ML) techniques for positioning, particularly in scenarios where traditional methods struggle due to NLOS or dense multipath effects.

The growing importance of location-based services has prompted 3GPP to dedicate significant efforts toward developing and standardizing advanced positioning techniques for 5G and 5G-Advanced networks, particularly from Releases (Rel.) 16 through Rel. 19. These initiatives aim to enable centimeter-level positioning accuracy, which is critical for a wide range of emerging applications, including autonomous driving, industrial automation, and augmented reality [14], [15]. To support this goal, 3GPP specified two dedicated positioning signals in Rel. 16: the PRS for downlink-based positioning and the sounding reference signal (SRS) for uplink-based methods. Rel. 17 introduced multipath reporting, time delay correction between receiver and transmitter, and LOS/NLOS identification where the LOS/NLOS likelihood is utilized to weight certain measurements for localization [15].

Rel. 18 expands upon these capabilities by introducing bandwidth aggregation to improve the effective bandwidth of the reference signal [16] and carrier phase positioning (CPP)—a highly precise technique that leverages the phase of radio frequency (RF) carrier waves to estimate the distance between user equipment (UE) and 5G base stations (BSs) [17]. By measuring the subtle phase shifts of these high frequency signals, CPP enables fine-grained distance estimation, making it a key enabler for achieving cm-level localization accuracy in next-generation networks.

Building on recent advancements in 5G positioning methodologies and the high accuracy enabled by carrier phase (CP) ranging, this paper proposes a terrestrial positioning system that operates over existing 5G infrastructure. The system is designed to localize UE based on CP measurements when at least three BSs maintain a LOS condition with the user. In scenarios where the LOS condition is momentarily disrupted, the system compensates by incorporating additional sensor data, such as inertial measurements from an inertial measurement unit (IMU) and visual odometry derived from a camera sensor. This study aims to demonstrate that modern 5G networks along with the fusion of complementary sensors data, can effectively serve as an alternative/complementary infrastructure to GNSS in providing accurate positioning services while providing redundancy to enhance the robustness and reliability of the localization systems.

While our primary objective is to showcase the feasibility of achieving accurate user localization using 5G networks in practical scenarios, we also elaborate on the technical challenges encountered during system development and the solutions we implemented. These challenges and corresponding methodologies are summarized below:

- **Carrier Phase Ranging and Integer Ambiguity Resolution:**

We leverage the high-precision nature of CP ranging for user localization in environments with multiple LOS-connected BSs. A critical challenge in CP-based positioning is resolving the integer ambiguity (IA)—the unknown number of full carrier wavelengths between the UE and BSs. Unlike many existing approaches that address this issue by relying on external radio access network (RAN) assistance or fusing CP with TDOA or carrier phase difference of arrival (CPDOA) data [4], [18], our method employs multi-frequency phase analysis for standalone IA resolution and improved phase noise reduction.

- **LOS/NLOS Classification Using ML:**

Since CP ranging assumes LOS propagation, the presence of NLOS conditions can degrade accuracy. However, prior knowledge of LOS condition is not available and needs to be obtained. To address this, we develop an ML-based LOS/NLOS classification module that analyzes channel impulse response (CIR) to differentiate between LOS and NLOS links in real time, enabling the system to selectively use only valid ranging data.

- **Sensor Fusion with Visual Odometry and IMU:**

When LOS connectivity is lost, the system transitions to using auxiliary sensors. In particular, a camera-based visual odometry module is used to estimate motion and po-

sition, which is then fused with the last known CP-based location using EKF. Additionally, IMU data is integrated into the EKF to further enhance positioning robustness and accuracy during CP signal outages. This external information is utilized until the LOS condition is resumed.

Above, we outlined our contribution to the development of an end-to-end positioning pipeline over 5G networks. The effectiveness of the proposed system is evaluated using the KITTI dataset [19], which features a vehicle equipped with a camera, an IMU, and a GPS sensor navigating through urban streets under varying channel conditions, including LOS and NLOS scenarios relative to BSs. The LOS/NLOS condition was evaluated based on a ray tracing tool called SIONNA [20]. Using the proposed methodology, we estimate the vehicle's position and compare it against the standard GNSS-based positioning services. Under LOS conditions with at least three BSs, the CPP achieves cm-level accuracy. In contrast, when LOS is obstructed, the system transitions to relying on visual odometry and IMU sensors, which effectively maintain continuous position tracking. This hybrid approach validates the system's capability to provide seamless localization even in challenging NLOS environments. Furthermore, we discuss the trade-offs, performance limitations, and practical considerations observed during these real-world evaluations, providing insights into the deployment feasibility and operational constraints of the proposed solution.

The rest of the paper is organized as follows. Section II provides a comprehensive literature review, outlining the key problems and summarizing existing solutions. Section III establishes the architecture of the proposed positioning and tracking system. Section IV offers an in-depth discussion on network planning and coverage, the characteristics of 5G channels, the structure of data and control signals. Section V introduces the theoretical foundations of CP ranging and details our proposed method for resolving the integer ambiguity. Section VI then focuses on LOS/NLOS classification, presenting our ML-based identification framework. In Section VII, we describe the integration of visual odometry and IMU data through a sensor fusion approach based on an Error-State Extended Kalman Filter (ES-EKF) and evaluate the performance of the proposed end-to-end positioning system, including a comparison with GNSS-based positioning services. Finally, Section VIII concludes the paper by summarizing our key findings and outlining directions for future work.

II. RELEVANT WORKS

The proposed positioning system comprises several key components, each contributing significantly to achieving a robust and highly accurate solution. This section breaks down these components and reviews relevant research associated with each.

A. Carrier Phase Positioning

As highlighted earlier, CPP forms the foundation of the proposed system. CPP has emerged as a pivotal technology for achieving cm-level accuracy in 5G-Advanced networks, driven

by its inclusion in 3GPP Rel. 18 as a key enabler for mission-critical industrial IoT (IIoT) and smart city applications such as precision asset tracking and augmented reality. The technical report [21] underscores CPP's feasibility through system-level simulations, demonstrating cm-level accuracy under line-of-sight (LOS) conditions [16]. However, practical implementations must deal with the ambiguity resolution challenge: the unknown integer number of full carrier cycles between UE and BSs. Recent works diverge in their approaches. For instance, Ou *et al.* [22] bypass direct ambiguity resolution by fusing TDOA with double-differenced CPDOA measurements. Their hybrid framework performs a localized search around TDOA-derived initial positions, mitigating clock offsets and phase wrapping effects through a weighted cost function. While computationally efficient, this method assumes reliable TDOA estimates—a limitation under severe multipath. In contrast, Deng *et al.* [23] tackle ambiguity resolution directly via double-differenced phase observations, isolating floating ambiguities using least-squares estimation and resolving integers through projection or Cholesky decomposition. Though rigorous, this approach introduces computational overhead, highlighting a key trade-off in CPP implementations. These challenges are also contextualized by Abuyaghi *et al.* The survey [24] presents ambiguity resolution algorithms and emphasize the need for robustness in non-ideal channel conditions—a concern echoed in [21].

However, despite these strides toward practical integration, the absence of holistic implementation frameworks persists—particularly for resolving ambiguities and validating performance in real-world deployments. Tools like the mixed-integer Cramér-Rao bound [25] have emerged to bridge theoretical models and practical parameterization, yet they alone cannot address the procedural void in end-to-end CPP pipelines. Recent works sidestep systematic guidance for integrating disparate techniques, such as signal acquisition, ambiguity resolution, and error correction, into cohesive positioning systems. Collectively, these efforts highlight CPP's maturation from theoretical promise to near-deployable capability. Nevertheless, the transition to ubiquitous cm-level positioning in 5G-Advanced networks hinges on unifying fragmented innovations into reproducible frameworks. Compared with the recent advancement *our approach eliminates dependencies on external RAN measurements by resolving carrier-phase ambiguities entirely through multifrequent phase analysis.*

B. LOS/NLOS Classification

While CPP offers superior precision compared to traditional time-based localization methods, its performance degrades significantly under NLOS conditions. As demonstrated in [14], phase errors increase from 1.4° in LOS to 3.4° in NLOS environments under the 3GPP indoor factory (InF) channel model, corresponding to distance errors of approximately 1.9 cm and 4.6 cm, respectively. To mitigate this degradation, assisted LOS/NLOS classification is essential.

Recent progress in ML has significantly improved the classification of LOS/NLOS signals—an essential step for achieving high-precision positioning. Unlike conventional techniques

that rely on simplified propagation assumptions and operate within low-dimensional feature spaces, ML approaches can extract and utilize features such as the CIR and Channel Frequency Response (CFR), as discussed in [26]. Supervised learning remains the predominant strategy, with ensemble-based models demonstrating LOS classification accuracies ranging from 65% to 95% in studies such as [27] and [28]. Deep learning has further advanced this field. For example, the GAN-autoencoder framework proposed in [26] achieves superior performance on imbalanced datasets, improving upon prior methods by 2.15–8%. Alternative approaches leveraging semi-supervised learning have also emerged. The study [29] uses a self-labeling strategy followed by supervised training of a Random Forest classifier to reduce mean localization error by up to 2.8 times. While effective, these methods can involve considerable computational overhead during the initial training phase.

In contrast to previous ML methods that primarily focus on mitigation during the localization process, our approach employs a simple yet effective detection-and-discard strategy. Rather than compensating for erroneous measurements during positioning estimation, *we proactively identify and exclude them beforehand*. Moreover, unlike traditional techniques that rely heavily on preprocessing and engineering statistical features—such as power delay profile (PDP) analysis—*our method operates directly on the raw received signal data, reducing complexity and potential sources of bias*. The model employs learned convolutional kernels to implicitly deconvolve channel effects, allowing it to distinguish meaningful signal components from channel-induced distortions, without the need for manually crafted features or predefined assumptions about channel characteristics. To ensure efficiency and suitability for real-time or resource-constrained applications, the proposed deep learning architecture is deliberately kept lightweight. It consists of a small number of convolutional layers for automatic feature extraction, followed by a compact fully connected network to perform channel condition classification.

C. Visual Odometry and Sensor Fusion for Positioning and Tracking

As part of the proposed positioning framework, we integrate both visual and inertial sensors to enhance the positioning robustness and reliability, especially in scenarios where CPP inputs are unavailable. Here, we review recent works that consider fusing IMU and visual sensor data for positioning.

Over the past decades, extensive research has been conducted on the integration of visual and inertial data for estimating pose—comprising position and orientation—a problem commonly referred to as visual-inertial odometry (VIO). VIO systems have been extensively applied in robotics, drones, and autonomous vehicles. State-of-the-art implementations such as [30]–[33] exemplify both filtering-based and optimization-based approaches. These systems typically rely on geometric constraints and known sensor models. Recently, learning-based VIO frameworks [34] have shown promise in improving estimation accuracy and robustness, especially under challenging visual conditions.

While these approaches deliver reliable short-term tracking, they are prone to cumulative drift in the absence of absolute references. To address this limitation, many methods incorporate additional sensors or map-based corrections to provide global constraints. More recently, several studies have investigated the fusion of wireless signal measurements—such as Wi-Fi, Bluetooth, UWB, and cellular signals [35]—as a means to mitigate long-term drift, offering an alternative to traditional map-based approaches for maintaining localization accuracy. However, such methods are often restricted to controlled indoor environments due to the scarcity of comprehensive real-world datasets that include wireless signal measurements.

Overall, sensor fusion has emerged as a central strategy for building resilient localization systems in environments where GNSS signals are degraded or absent. Combining multiple sensor modalities—including inertial measurements, visual features, and radio signals—significantly enhances accuracy, robustness, and continuity. *To this end, we propose a positioning system that fuses visual odometry, inertial measurements, and CPP data using an ES-EKF.*

III. SYSTEM DESIGN

This section presents a high-level overview of the proposed robust positioning framework, which integrates CPP in accordance with 3GPP standards, alongside a complementary sensor fusion module, as depicted in Fig. 1. While the system design aligns with the existing 3GPP positioning architecture, it is augmented with a fusion layer that incorporates visual odometry and IMU data to enhance reliability and continuity. This integration enables accurate and consistent position estimation, particularly in scenarios where LOS measurements are temporarily unavailable or degraded.

The 3GPP defines a modular positioning architecture consisting of the next-generation RAN (NG-RAN), the location management function (LMF), and the access and mobility management function (AMF), each with distinct responsibilities in enabling scalable and accurate localization. The NG-RAN comprises gNodeBs (gNBs), which transmit and receive dedicated positioning signals—PRS for downlink-based measurements and SRS for uplink-based measurements. The LMF, residing in the 5G Core (5GC), handles deployment-aware signal configuration and scheduling, collects measurement reports, and executes positioning algorithms. The AMF, also part of the 5GC, facilitates control-plane signaling, including configuring and coordinating positioning procedures between the LMF, NG-RAN, and UE.

The proposed design incorporates a CPP-based localization module that operates natively within the 3GPP framework using standard PRS and SRS signals. The system avoids the complexity of integer ambiguity resolution by using virtual wavelength processing, enabling efficient single-epoch position estimates. This approach ensures seamless integration with existing 5G NR protocols and infrastructure.

To support the precision of CPP in realistic propagation conditions, our system integrates a LOS/NLOS classification layer that filters measurements before positioning. Implemented as a lightweight deep learning model operating on

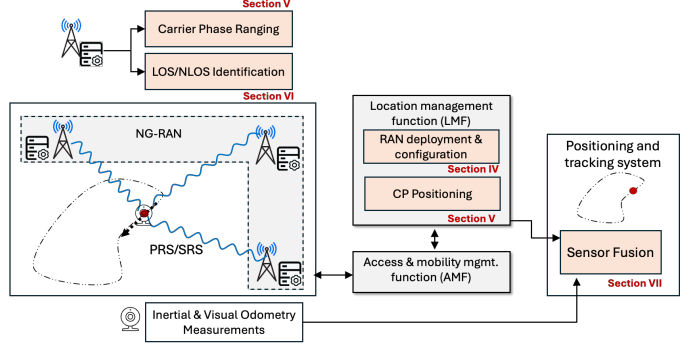


Fig. 1. System-level depiction of the designed positioning and tracking system. The focused areas of the paper contributions, along with the relevant sections, are also shown.

SRS-derived CIRs, this component selectively admits only high-confidence LOS measurements. Its modular placement within the architecture allows for real-time classification of CP measurements.

Complementing the CPP engine, the sensor fusion module is designed to maintain positioning continuity during periods of degraded LOS visibility. By combining stereo visual odometry with IMU measurements in an ES-EKF, this module enables drift-resilient trajectory estimation. Its loosely coupled integration allows it to operate independently when needed while remaining synchronized with CPP when LOS signals become available again.

The design uses ray-tracing simulations (e.g., via Sionna) to evaluate LOS coverage along anticipated tracks for a selected gNB deployment configuration, which serves as the basis for determining the effectiveness of sensor fusion in LOS-deprived scenarios.

By embedding our proposed CPP-based positioning method, LOS/NLOS classifier, sensor fusion capability, and deployment-aware management into the standard 3GPP architecture, we provide a robust, scalable, and centimeter-level accurate localization solution. This integrated approach ensures both the precision of CP-based positioning and the robustness required for practical, real-world deployments.

IV. RAN DEPLOYMENT AND CONFIGURATION FOR HIGH-PRECISION POSITIONING

All generations of RAN prior to 6G [36], [37] were designed primarily to support enhanced communication services, with localization considered a secondary feature [38]. Therefore, adapting RAN for high-precision, robust positioning requires specific adjustments to deployment and signaling configurations. These adjustments include deploying gNBs to improve LOS visibility during the RAN planning phase, and configuring physical layer (PHY) signals appropriately for high-resolution measurements.

A. Network Coverage Planning

Traditionally, a reliable network requires optimizing two key metrics during the planning phase: coverage and capacity. Effective radio network planning focuses on maximizing

the signal-to-interference-plus-noise ratio (SINR) by minimizing inter-BS interference and eliminating coverage gaps. To achieve these goals, RF planning aims to minimize the overlap between the coverage footprints of adjacent BSs.

However, achieving high-precision positioning introduces additional requirements. Accurate positioning depends on the direct (i.e., LOS) reception of RF signals from multiple BSs [17]. Therefore, cellular network planning for positioning must prioritize BS placement to maximize LOS conditions. This dual optimization highlights the trade-off between minimizing interference for communication and ensuring sufficient LOS signal diversity for positioning. Alternatively, single-purpose PRS- or SRS-only transmission-reception points (TRPs), as described in [39], can be deployed.

To illustrate the contrasting requirements of RF coverage planning for communication and positioning, we performed ray-tracing simulations using Sionna [20]. The resulting coverage levels for communication and positioning are shown in Fig. 2 and Fig. 3, respectively.

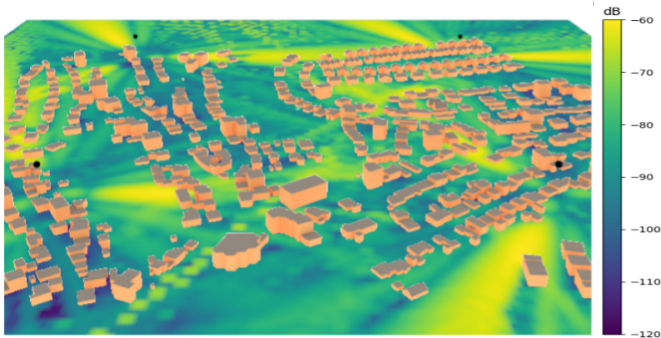


Fig. 2. Simulated RF coverage in a suburban environment using four BSs. The map shows path gain levels in dB, calculated via ray-tracing including LOS, reflection, and diffraction effects.

Fig. 2 shows a simulated RF coverage map for the suburban residential area in which the KITTI dataset [19] was collected, covering an area of 900 m×800 m. Four BSs were positioned at a height of 30 m—above rooftop level—and tilted downward by 6°. The simulation was performed using 3D building models and a ray-tracing engine that accounts for LOS, reflection, and diffraction effects. The resulting coverage map displays path-gain values on a 5 m×5 m grid. As shown, the four BSs provide sufficient coverage across the entire area.

In contrast, Fig. 3 illustrates the LOS visibility requirement for high-accuracy positioning, where a minimum of three BSs are in LOS. The simulation considered only direct LOS propagation, excluding reflection and diffraction effects. Following the simulation, each 5 m×5 m grid cell was analyzed to determine how many BSs had a direct LOS path to that location. Blue grid cells indicate areas where at least three out of four deployed BSs simultaneously provides LOS coverage. In this scenario, only 16% of the total area meets this requirement. These results emphasize the need to reconsider RF planning strategies when accurate positioning is a primary design goal.

To improve positioning coverage, we propose a denser deployment strategy tailored specifically for localization rather than conventional communication requirements. By increasing the number of BSs from four to twelve (depicted by

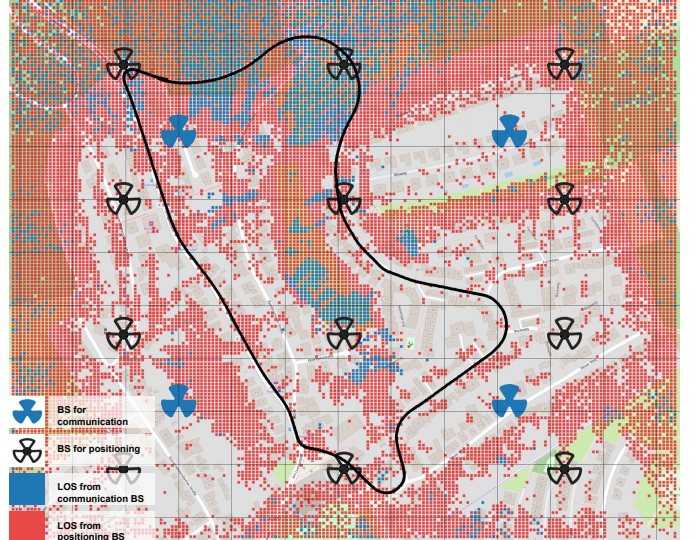


Fig. 3. Compares two network planning strategies: (1) The four blue cake-shaped symbols represent a conventional deployment designed primarily for communication services, resulting in limited LOS coverage—blue grid cells indicate regions with LOS to at least three BSs. (2) In contrast, the twelve black cake-shaped symbols correspond to a network layout optimized for localization, where positioning is treated as a primary service.

black markers), LOS coverage to at least three BSs rises to approximately 64% of the area. This enhanced layout meets the typical conditions required for accurate carrier-phase positioning, thereby demonstrating the importance of RF planning with localization objectives in mind.

When the objective is to enable high-precision positioning, simulation tools should be employed to determine the optimal placement of BSs, maximizing LOS probability throughout the coverage area. Despite the increased BS density, the simulation reveals several zones that still lack LOS visibility to three or more BSs. This highlights the importance of preprocessing algorithms capable of distinguishing LOS from NLOS paths, as well as the need to integrate sensor fusion techniques to enhance the robustness and accuracy of positioning solutions.

B. 5G NR PHY Channels and Signals suitable for Positioning

A fundamental requirement for any positioning system is prior knowledge of the signals used for localization. In the NR PHY structure, several channels and signals with deterministic properties are identified.

These include the NR common signals, synchronization signal block, and channel state information reference signal, which are used primarily for communication, as well as positioning-specific signals.

To support improved positioning accuracy, 3GPP has specified two dedicated signals: PRS and SRS. PRS is a downlink, single-purpose positioning signal, while SRS is primarily used for uplink channel measurements. Starting with 3GPP Rel. 16, the SRS is explicitly engineered to support positioning in addition to its original channel-sounding role.

1) *PRS Characteristics—Periodicity, Muting, and Sequence Generation:* PRS is designed to overcome limitations in

common reference signals, such as interference and poor correlation properties. This purpose-specific design improves the positioning, at the expense of introducing downlink communication overhead. PRS characteristics are highly configurable in time, bandwidth, and comb pattern allocation within the Physical Resource Block (PRB) as described in [40].

The network can tune PRS by adjusting the configuration parameters: (i) the transmission period (4–10240 slots); (ii) the number of consecutive OFDM symbols per slot; (iii) the occupied bandwidth (24–272 PRBs, in 4-PRB steps); (iv) the comb size, i.e., the number of subcarriers in each PRB that carry PRS; (v) a binary muting pattern of length 2–32 that improves SINR by coordinating gaps among cells; and (vi) one of 4096 Gold-sequence IDs [41].

PRS is specifically configured to ensure high Resource Elements (REs) density, improving positioning accuracy and detectability. However, the additional overhead caused by data transmission and the requirement for coordination among multiple BSs makes PRS optional/rare in commercial communication-oriented networks.

2) *SRS Characteristics– Periodicity, Scheduling, and Sequence Generation:* Similar to the PRS, 3GPP introduced SRS as an uplink signal for channel quality estimation and positioning purposes. SRS is configured individually for each UE to support channel estimation for communication. However, when used for positioning, it supports customized, positioning-specific configurations.

Key SRS parameters for positioning include [39]–[41]: (i) periodicity and timing, where operators choose the number of OFDM symbols and triggering mode (periodic, semi-persistent, or on-demand) to balance uplink load against update rate; (ii) bandwidth, selected from the resource sets listed in [41, Table 6.4.1.4.3-1]; (iii) comb spacing, with subcarrier densities of 2, 4, or 8; (iv) tight scheduling so that multiple BSs receive the UE’s SRS in the same time-frequency resource; and (v) sequence IDs, drawn from up to 65535 Zadoff–Chu sequences for orthogonality.

Fig. 4 illustrates an example of SRS configurations within the NR OFDMA time-frequency grid. It shows the SRS allocation within a single PRB, highlighting the occupied OFDM symbols and subcarriers based on a comb-type structure. SRS resources are allocated to a single UE by the gNodeB scheduler. Other UEs within the coverage area can be allocated similar SRS resources by applying different time and frequency shifts.

By configuring SRS with positioning-centric parameters (e.g., higher bandwidth or denser comb spacing), networks can enhance the accuracy of UL-based positioning methods. However, similar to PRS, these uplink-specific SRS configurations require additional uplink resources and coordination among BSs, balancing the trade-off between communication throughput and high-precision localization.

Both PRS and SRS can be generated using stable reference sequences and tightly controlled timing, making them well-suited for CP-based positioning. Their deterministic properties support high-fidelity phase measurements, enabling the subwavelength accuracy required for advanced, cm-level positioning.

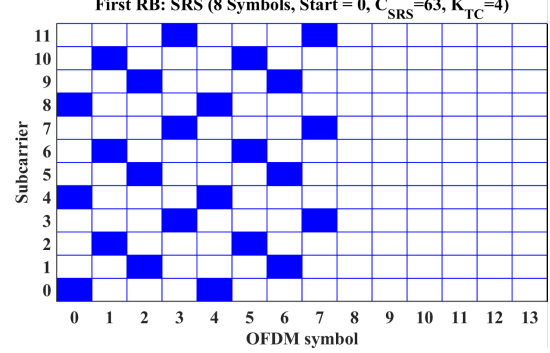


Fig. 4. Example SRS configuration within the NR OFDMA grid. SRS allocation within a single PRB, illustrating comb-based subcarrier mapping across OFDM symbols.

V. CARRIER PHASE POSITIONING IN CHALLENGING PROPAGATION ENVIRONMENTS

We propose a CP-based positioning framework for 5G NR systems, designed to meet the stringent accuracy requirements of industrial and commercial applications across both FR1: 0.41–7.125 GHz and FR2: 24.25–52.6 GHz, as specified in 3GPP Rel. 18 [42]. While initially targeting InF deployments, the methodology addresses general harsh propagation environments, including urban microcells (UMi), indoor offices (InO), and other scenarios characterized by dense clutter, NLOS, and dynamic obstacle configurations per 3GPP TR 38.901 channel models [43].

The proposed CPP approach shares fundamental technical challenges with GNSS solutions [44], particularly IA resolution and multipath-induced phase errors. However, NR systems provide distinct advantages through controlled BSs deployments and multi-subcarrier capabilities that are unavailable in satellite navigation. Additionally, NR systems offer improved error mitigation techniques such as LOS/NLOS identification, enhancing the reliability and robustness of CP measurements. These capabilities support the application of CPP both as a standalone solution and as an enhancement to legacy NR positioning methods based on timing, angle, and power measurements, significantly improving overall accuracy.

CP measurements fundamentally determine the phase shift between an incoming carrier signal and a receiver’s predefined reference phase (Fig. 5). The measured phase shift is confined to $[0, 2\pi)$ radians (or equivalently mapped from $[-\pi, \pi)$), with errors typically limited to a small fraction of the signal wavelength [45]. Under LOS conditions, this enables precise distance calculation through linear phase-to-distance conversion, allowing cm-level positioning accuracy [46]. However, three critical limitations arise: (1) strict synchronization requirements between transmitter and receiver for phase comparison validity, (2) dependence on LOS/semi-LOS propagation to avoid multipath-induced distortions and timing ambiguities (NLOS scenarios degrade precision by orders of magnitude), and (3) the fundamental IA problem—the inability to resolve the integer number of full wavelength cycles (N) preceding the measured fractional phase. These constraints collectively challenge CPP’s reliability in NLOS environments, despite its theoretical advantages for industrial/urban applications.

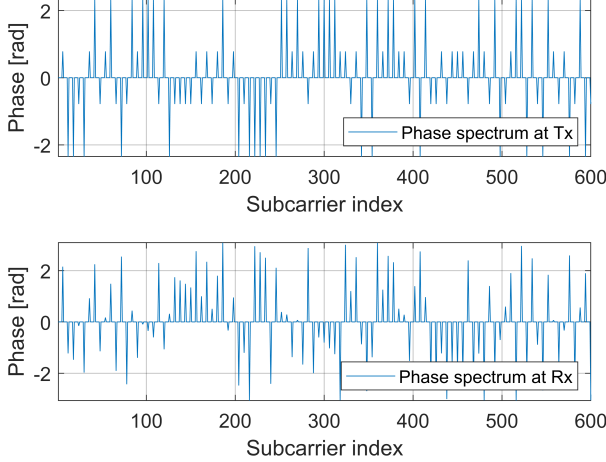


Fig. 5. Phase spectrum at the transmitter and receiver, showing the phase shifts resulting from the propagation and communication channel.

A. Virtual wavelength

The challenge of synchronization, specifically addressing the phase offset between transmitter (Tx) and receiver (Rx), can be mitigated by using differential measurements. By analyzing the phase difference $\Delta\phi = \phi_2 - \phi_1$ between two carriers of wavelengths λ_1 and λ_2 propagating in free space, a virtual wave is created (Fig. 6). The wavelength of such a virtual wave, denoted as λ_v , is determined by the formula:

$$\lambda_v = \frac{1}{\frac{1}{\lambda_2} - \frac{1}{\lambda_1}}. \quad (1)$$

The ranging method, essential for CPP operation, is based on the principle that the differential phase corresponds to the distance traveled by the virtual signal. This is achievable because the diverging phase differences between the two subcarriers generate the phase of a virtual wave, which behaves identically to that of real signal propagation:

$$d = \left(\frac{\Delta\phi}{2\pi} + N \right) \lambda_v, \quad (2)$$

where N is the unknown integer that must be determined within a range of possible solutions.

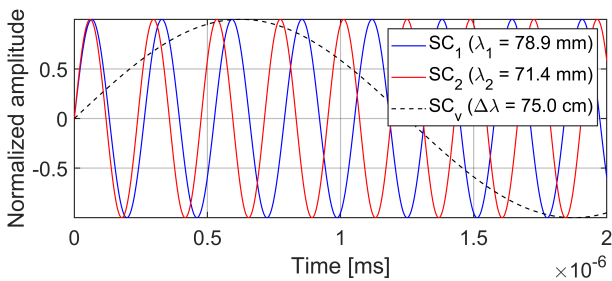


Fig. 6. Virtual wave from phase difference $\Delta\Phi$ of two subcarriers SC_1 and SC_2 .

By substituting frequency for wavelength in (1), it can be demonstrated that the virtual wavelength is directly influenced by the frequency difference Δf of the used subcarriers:

$$\lambda_v = \frac{1}{\frac{f_2}{c} - \frac{f_1}{c}} = \frac{c}{\Delta f}. \quad (3)$$

In this context, Δf corresponds to the subcarrier spacing (SCS). Consequently, the differential analysis of any subcarrier pair spaced by a constant integer $k \cdot SCS$ results in a virtual wave with a consistent wavelength. This property allows for the adjustment of the virtual wavelength by k and facilitates averaging across the allocated bandwidth, as outlined in [47].

B. Solution outline

Considering the comb-pattern of subcarrier allocation in the resource block for the PRS or SRS, let us assume that we have K subcarriers at our disposal. To perform a differential phase analysis, we introduce a spacing of k subcarriers, where $0 < k < K/2$. By performing a pairwise sweep over all subcarriers, we generate $K - k$ phase differences, denoted as $\Delta\phi_i = \phi_{i+k} - \phi_i$, for $i = 1, \dots, K - k$. These phase differences are then averaged to enhance the robustness of the analysis, reduce the impact of noise across subcarriers, and improve the reliability of the phase estimate.

In the approach described by [47], the averaging process is performed by calculating the phase of the vector sum of the complex frequency coefficients. Specifically, since phase differences are directly derived from the complex representations of the subcarriers, this vector summation is both straightforward and computationally efficient. Mathematically, the approach is expressed as follows:

$$\Delta\phi_{avg} = \arg \left(\sum_{i=1}^{K-k} A_{i+k} e^{j\phi_{i+k}} - A_i e^{j\phi_i} \right), \quad (4)$$

where $\Delta\phi_{avg}$ is the average phase difference and $A_i e^{j\phi_i}$ denotes the complex exponential form of the i -th subcarrier. Although this method is computationally optimal, it has some limitations:

- The noise originating from subcarriers not allocated in the comb-pattern typically carries small amplitudes. This noise directly affects the phase result, which is insignificant when the noise follows a zero-mean distribution. In practical scenarios where noise may not be evenly distributed, this assumption does not always hold.
- Environmental factors that lead to uneven amplitude variations across allocated frequencies cause individual subcarriers to contribute disproportionately to the overall averaging process. This imbalance may compromise the robustness of the phase-averaging method.

To address these limitations, we propose an alternative approach in which the first step involves excluding unallocated subcarriers, which are known to carry only noise. The n -sized comb-pattern of subcarrier allocation is predefined, allowing for the identification of subcarriers actively allocated for signal transmission. After excluding the unallocated subcarriers, only the phase of the remaining is extracted and processed through averaging, resulting in a more robust phase estimate that is less susceptible to noise artifacts and amplitude fluctuations:

$$\Delta\phi_{avg} = \left[\frac{n}{K - k} \right] \left(\sum_{i=0}^{\lceil (K-k)/n \rceil - 1} \arg (A_{in+k} e^{j\Delta\phi_{in+k}}) - \arg (A_{in} e^{j\Delta\phi_{in}}) \right), \quad (5)$$

To correctly apply (5), the subcarriers must share a common initial phase. This necessitates correcting the phase shifts introduced by the pseudorandom code structure of the transmitted PRS/SRS signals. These shifts are deterministically defined by the code structure and can be calculated at both Tx and Rx. Once corrected, as shown in Fig. 7, reliable phase differentiation can be performed.

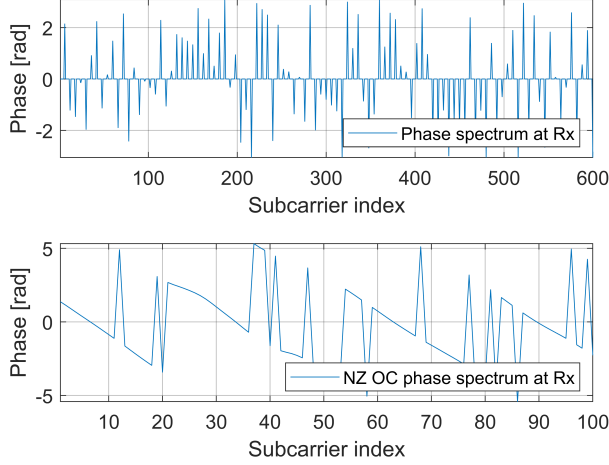


Fig. 7. Phase spectrum at the receiver after phase offset correction and exclusion of unallocated subcarriers. In the legend, NZ OC stands for non-zero offset corrected.

The second crucial step is to address the mutual phase relationships between subcarriers during the subtraction process. These phase relationships are measured within the range $(-2\pi, 2\pi]$. Simple differentiation, with phase wrapping in the range $(-\pi, \pi]$, does not inherently consider the direction of phase changes, potentially leading to positive and negative differences. In this scenario, we ensure that the subcarrier with the higher index (corresponding to a higher frequency) always has a phase that is ahead of the preceding subcarrier (phase progression). This guarantees that the phase difference remains consistently with the expected subcarrier physics (Fig. 8), and enhances the reliability of the measurement process.

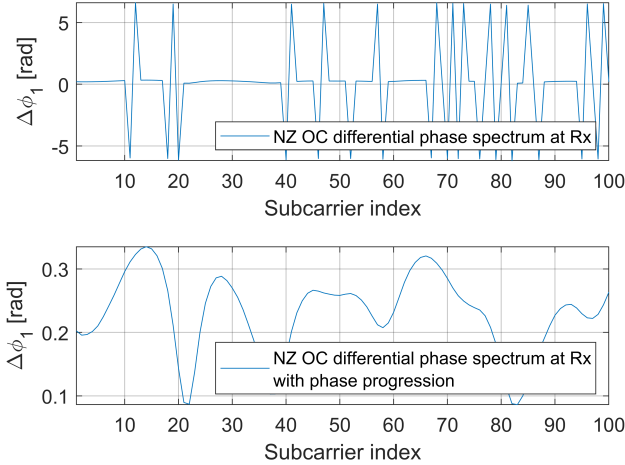


Fig. 8. Phase spectrum at the receiver after phase offset correction and exclusion of unallocated subcarriers, with phase progression included.

By adopting this approach alongside the use of (5) in place

of (4), the error variance is reduced, leading to enhanced measurement precision and more reliable results.

The unresolved issue lies in determining the value of N in (2), which corresponds to the solution of the IA problem. By selecting an appropriate k , we can control the virtual wavelength. For example, choosing the minimum spacing with $k = 1$ maximizes λ_v . In the 400 MHz band, using a SCS of 120 kHz results in a virtual wavelength of approximately 404 m. In InF/UMi measurements, where distances are typically much shorter, we can reasonably assume that the Rx is less than one wavelength away from the Tx. Under this assumption, $N = 0$, and the IA problem does not need to be resolved. However, when phase measurements are taken within the range $(-\pi, \pi]$, the limited measurement resolution and phase noise introduce errors as fractions of the wavelength. Therefore, a shorter λ_v is favorable, as it results in smaller distance errors and improves accuracy.

When maximizing the spacing of differentiated subcarriers, such as with $k = K/2$, the resulting virtual wavelength is approximately 1.5 m (400 MHz bandwidth, 120 kHz SCS). However, in this case, N remains unresolved. To address this, following the approach in [47], the result can be calculated based on $\Delta\Phi_{K/2}$ using the measurement of $\Delta\Phi_1$. A similar strategy is commonly employed to reduce the search space for N in single-phase measurements by supplementing with TOA [4]. Notably, the proposed CPP method relies solely on averaging the phase differences measured within a single FFT frame but with a varied spacing of k . This intrinsic approach simplifies implementation while maintaining accuracy.

The adjustable and more flexible approach enables wavelength shortening tailored to a known BS deployment, considering the maximum possible distance between Tx and Rx and the constraints of determining the distance using a single k . The measurement can be extended to cover the full range of possible k values in scenarios with strong, non-uniformly distributed phase noise. Measurement accuracy can be significantly improved by using intermediate results and analyzing differences in phase noise realizations obtained for the individual k . This approach is particularly beneficial in critical cases, as it combines the results of multiple distances calculated for $\Delta\Phi_i$, where $i = 1, 2, \dots, K/2$, to mitigate the effects of noise and enhance the robustness of the measurement process.

C. Simulation Scenario for 3GPP Urban Microcell (UMi)

We designed an example simulation scenario using the QUADRIGA framework to evaluate the CPP positioning method in a 3GPP-compliant UMi environment. The setup adheres to [43, Section 7.2] with the following key parameters:

- Carrier frequency: 3.8 GHz (mid-band 5G NR)
- Bandwidth: 100 MHz
- Subcarrier spacing: 30 kHz
- Antenna: Omnidirectional at TRPs and UE

Three TRPs are deployed asymmetrically with inter-site distances (ISDs) of 50–70 m, compliant with the non-ultra-dense UMi range (50–200 m ISD) [43, Table 7.2-1]. The TRP locations are as follows:

- TRP-1: (100, 100, 10) m (street-level deployment)
- TRP-2: (150, 90, 10) m
- TRP-3: (140, 150, 10) m

UE is initialized at coordinates (120, 110, 1.5) m, and mobility is simulated at 3 km/h using a random waypoint model to represent low-speed urban movement. SRS sequences are generated for 3276 subcarriers using a comb-6 configuration with 8 symbols per frame, while the channel impulse response incorporates UMi-specific delay spreads as defined in [43, Table 7.5-6].

The geometry-based channel model incorporates frequency-dependent path loss exponents derived from [43, Table 7.4.1-1]. The LOS probability follows the piecewise function defined in [43, Table 7.4.2-1]. Urban-specific effects such as clutter loss (10 dB for street canyons) and outdoor diffraction are included to model signal attenuation in dense environments. The parameters align fully with QUADRI Γ GA's 3GPP UMi channel model implementation as it natively supports:

- The LOS probability formula and path loss exponents from 3GPP TR 38.901 [43],
- Clutter loss and street canyon effects via its `clutter_density` parameter,
- Delay/angular spread distributions for UMi NLOS conditions.

The asymmetric TRP layout and UE mobility model are configurable through QUADRI Γ GA's `qd_layout` and `qd_track` classes, ensuring reproducible results for UMi studies.

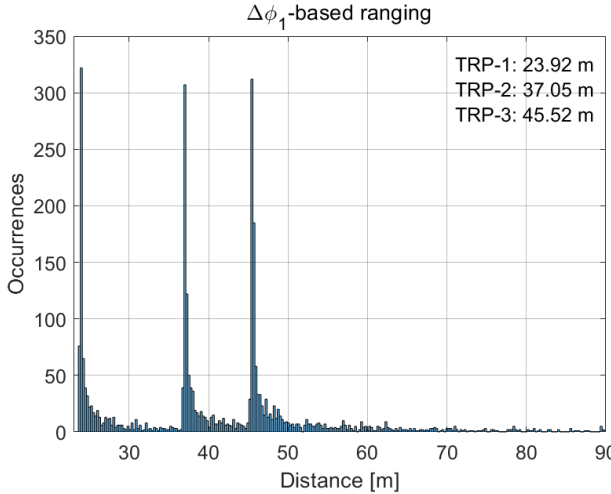


Fig. 9. The Euclidean distances of the receiver to each of the transmitters.

The experimental evaluation, conducted over 10^3 iterations, reveals critical insights into ranging precision through combined distance analysis (Fig. 9). The three-dimensional (3D) distance estimation to each TRP demonstrates three distinct histogram peaks at ~ 23.9 m, ~ 37.1 m, and ~ 45.5 m (± 10 cm resolution), corresponding precisely to simulated UE-TRP geometries. However, high-accuracy CP measurements (≤ 10 cm precision) are achieved in only $\sim 30\%$ of cases – LOS conditions with high signal quality, while NLOS conditions exhibit characteristic heavy-tailed error distributions.

Attaining centimeter-level positioning accuracy fundamentally requires simultaneous high-precision ranging to ≥ 3 TRPs

TABLE I
POSITIONING ERROR FOR LOS AND MIXED LOS/NLOS CONDITIONS IN UMI SCENARIOS

Percentile	2D		3D	
	LOS	LOS/NLOS	LOS	LOS/NLOS
90%	23.4 cm	68.9 m	67.5 cm	75.3 m
80%	18.3 cm	48.3 m	54.4 cm	59.1 m
70%	15.2 cm	33.0 m	47.1 cm	46.5 m

under LOS propagation. This geometric constraint introduces critical performance limitations, as evidenced by the 90th percentile error reduction from 68.9 m to 23.4 cm in horizontal (2D) scenarios through NLOS exclusion (Table I). The positioning framework implements multi-ranging over symbols within a single transmission frame using best-measurement selection from participating TRPs, with trilateration errors constrained to < 100 m—a practical limit derived from the 70 m transmitter grid spacing in our UMi deployment scenario.

The results demonstrate that even isolated NLOS errors disproportionately degrade multilateration accuracy, underscoring the critical need for robust NLOS identification and exclusion (detailed in Section IV-A and Fig. 12). Achieving reliable cm-level positioning in mixed environments requires two key enablers: 1) ML-assisted NLOS mitigation, and 2) geometric diversity that ensures concurrent LOS visibility to ≥ 3 spatially distributed TRPs.

VI. LOS AND NLOS LINK CLASSIFICATION

As previously discussed, LOS/NLOS classification can significantly improve CPP accuracy. To enable this, we employ a supervised deep learning (DL) approach using a convolutional neural network (CNN) trained on data from the simulation setup in Sec. V-C. The model takes as input the time-domain SRS waveform measured at the receiver, which reflects channel effects through the CIR. This waveform, after fast Fourier transform (FFT), corresponds to 3276 complex values¹, which are batch-normalized in the *Sequence Input* layer, eliminating the need for further preprocessing. The output layer is a fully connected layer with two neurons corresponding to LOS and NLOS classes, followed by a Softmax activation for binary classification.

Since QUADRI Γ GA uses probabilistic modeling for LOS/NLOS generation, the true channel state is not directly available. To label the data, we use the known Tx and Rx positions to compute the true propagation delay τ_{tr} from geometric distance, as defined in (6), where c is the speed of light.

$$\tau_{true} = \frac{\|\mathbf{P}_{tx} - \mathbf{P}_{rx}\|}{c} \quad (6)$$

In contrast, the estimated delay τ_{est} can be obtained from the PDP of a received SRS signal. Specifically, τ_{est} corresponds to the delay associated with the strongest multipath component, as defined in (7). Consequently, the absolute difference between the estimated and true delays is calculated as in (8).

$$\tau_{est} = \arg \max_{\tau} PDP(\tau) \quad (7)$$

¹This corresponds to 273 physical resource blocks (PRBs), each consisting of 12 subcarriers, giving a total of $273 \times 12 = 3276$ subcarriers. At 30 kHz spacing, this yields ≈ 98.28 MHz, approximating the 100 MHz SRS bandwidth in 5G NR.

$$\tau_{\text{diff}} = |\tau_{\text{est}} - \tau_{\text{true}}| \quad (8)$$

The absolute delay difference is compared to a threshold of approximately 10 ns—equivalent to one symbol duration based on system bandwidth—to classify the SRS as LOS or NLOS. If τ_{diff} exceeds the above threshold, the instance is labeled as NLOS; otherwise, LOS. The labeled data, along with the corresponding SRS waveforms, are then prepared as input-output pairs for the DL model.

For the classification task, our primary approach involves estimating a convolutional kernel that effectively deconvolves channel effects from the useful signal. Consequently, convolutional layers are adopted within the DL architecture to facilitate feature extraction related to these channel characteristics. Following convolutional processing, fully connected (dense) layers progressively learn to predict accurate labels based on the extracted features. The detailed structure of the final DL model and its layers is provided in Table II.

TABLE II
NEURAL NETWORK ARCHITECTURE SUMMARY

Type	Description
Sequence Input	Sequence input with 1 dimension
1-D Convolution	64 filters of size 16x1, stride 2, 'same' padding
Batch Normalization	Batch normalization 64 channels
ReLU	ReLU activation
1-D Convolution	32 filters of size 8x64, stride 2, 'same' padding
Batch Normalization	Batch normalization 32 channels
ReLU	ReLU activation
Global Average Pooling	1-D global average pooling
Fully Connected	Fully connected layer 64 outputs
ReLU	ReLU activation
Fully Connected	Fully connected layer w32 outputs
ReLU	ReLU activation
Fully Connected	Fully connected layer 2 outputs
Softmax	Softmax activation

In this work, the model is trained using *adam* optimizer, with an initial learning rate of 0.001. An L2 regularization factor of 0.0001 is used to penalize abnormal weights during the training. To avoid divergence, a piecewise learning rate scheduler is used. This strategy is used during model training, where the learning rate is adjusted at predefined intervals (epochs), often reduced by certain factors after specified training periods. This method helps improve model convergence by allowing larger initial steps followed by smaller refinements. The dropout factor and dropout period of the scheduler are configured to 0.6 and 5, respectively. Additionally, an early stopping mechanism is implemented by 10 consecutive validation epochs to control the model's generalizability.

The DL training performance is illustrated in Fig. 10. As depicted, the trained model achieves a performance exceeding 90% for both accuracy and ROC-AUC metrics. Accuracy measures the proportion of correctly predicted labels relative to the total number of predictions, while ROC-AUC provides a measure of the model's ability to distinguish between LOS and NLOS scenarios across various threshold settings. Consequently, the ROC-AUC metric is specifically included to offer insight into model robustness and discriminative capability. Additionally, the loss function, the residual error reduction between the model's predicted output and the true target in each iteration, is depicted, showing that the algorithm converges to its local optimum.

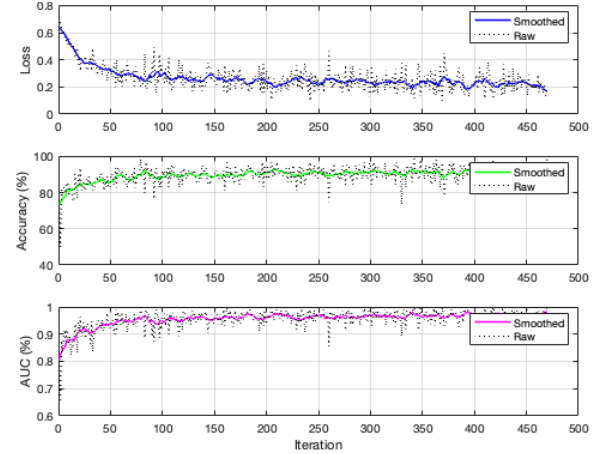


Fig. 10. DL classifier performance in terms of accuracy and auc, smoothed by a sliding window of 10 steps

The confusion matrix in Fig. 11 presents the performance of the DL model on unseen data. Notably, the model achieves higher accuracy in classifying NLOS links compared to LOS. This outcome is favorable, as reliable positioning depends critically on accurately identifying and excluding NLOS links. Minimizing false negatives—i.e., instances where NLOS links are mistakenly classified as LOS—is particularly important to ensure the robustness of the positioning system.

		Predicted	
		LOS	NLOS
Actual	LOS	164 (85.9%)	27 (14.1%)
	NLOS	12 (7.1%)	157 (92.9%)

Fig. 11. DL prediction accuracy, normalized by rows

Leveraging the high accuracy of our NLOS detection model, we apply the trained DL network to label incoming signals prior to CPP execution. We then evaluate the impact of discarding NLOS links on positioning accuracy. Fig. 12 presents the cumulative distribution function of 2D and 3D positioning errors across three scenarios: (i) only LOS links, (ii) a mix of LOS and NLOS links, and (iii) a mixed scenario where the DL model is used to identify and exclude NLOS links. The results show that using DL-based NLOS filtering significantly reduces positioning error, bringing the performance close to that of the pure LOS case.

VII. SENSOR FUSION WITH INTEGRATED CARRIER PHASE POSITIONING

To ensure robust and high-precision localization under dynamic motion, variable visibility, and LOS/NLOS channel transitions, we integrate information from multiple complementary sensors. Specifically, we integrate inertial measurement data and stereo visual odometry with CPP-based positioning technique. The fusion framework is implemented using an ES-EKF, which provides a principled probabilistic

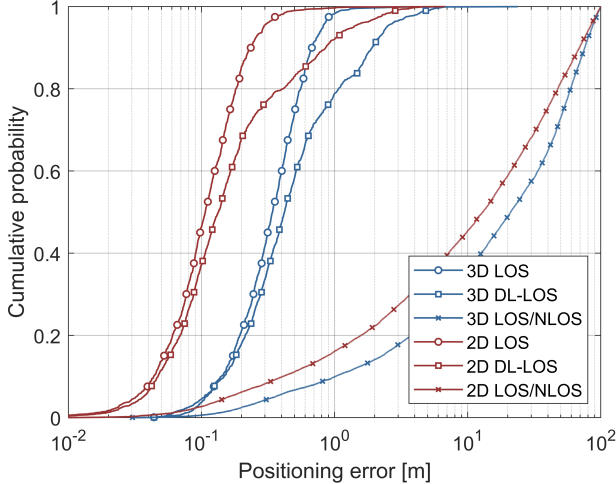


Fig. 12. Cumulative distribution function of 2D/3D positioning errors under LOS-only, mixed LOS/NLOS conditions, and DL-assisted LOS identification with NLOS mitigation in UMi scenarios.

framework for integrating sensor data with different noise characteristics and availability, including visual odometry, inertial measurements, and CPP updates that may be intermittent due to varying LOS/NLOS conditions.

A. Visual Odometry

Visual odometry (VO) is a method that uses sequential image data from a camera sensor to compute and estimate motion. The motion of the agent is tracked across multiple sequential frames, essentially providing information on the agent's trajectory. The VO system used in this work is a feature-based stereo-visual odometry. Knowing the starting position, we can then track the agent's motion across the map. By the application of RANSAC (RANdom SAmple Consensus) based outlier detection system, the influence of dynamic moving objects on the computation is reduced, and the reliability of the visual odometry estimates is increased. This is because the estimate of the motion is highly susceptible to the environment. This susceptibility arises from the fact that dynamic elements in the environment can corrupt the motion estimation by introducing extraneous motion components that are incorrectly attributed to the agent.

B. Inertial Odometry

Inertial sensors can measure the acceleration and angular velocity of an agent. However, estimating motion solely based on these measurements is highly error-prone due to sensor bias, noise, and integration drift over time. Although displacement can be derived from velocity and time using the basic laws of motion (i.e., kinematic equations), such calculations are highly sensitive to sensor errors, making them unreliable when relying on inertial sensors alone. Despite these limitations, inertial data remains valuable in sensor fusion systems. Over short time intervals, motion estimates derived from inertial sensors are sufficiently accurate to provide useful complementary information that enhances the overall robustness and precision of fusion-based motion estimation.

C. Error State Extended Kalman Filter

The proposed ES-EKF filter estimates the agent's state, consisting of the 3D position $\mathbf{p} \in \mathbb{R}^3$, velocity $\mathbf{v} \in \mathbb{R}^3$, and orientation $\mathbf{q} \in \mathbb{R}^4$. The state vector at time step k is defined as $\mathbf{x}_k = [\mathbf{p}_k^T, \mathbf{v}_k^T, \mathbf{q}_k^T]^T \in \mathbb{R}^{10}$. Using the nonlinear motion model, we propagate/predict the nominal state as:

$$\mathbf{p}_k = \mathbf{p}_{k-1} + \Delta t \cdot \mathbf{v}_{k-1} + \frac{\Delta t^2}{2} \cdot (\mathbf{R}(\mathbf{q}_{k-1}) \cdot \mathbf{f}_{k-1} + \mathbf{g}) \quad (9)$$

$$\mathbf{v}_k = \mathbf{v}_{k-1} + \Delta t \cdot (\mathbf{R}(\mathbf{q}_{k-1}) \cdot \mathbf{f}_{k-1} + \mathbf{g}) \quad (10)$$

$$\mathbf{q}_k = \mathbf{q}_{k-1} \otimes \mathbf{q}(\omega_{k-1} \Delta t) \quad (11)$$

where \mathbf{p}_{k-1} , \mathbf{v}_{k-1} , and \mathbf{q}_{k-1} represent the previous position, velocity, and orientation states, respectively. Δt represents the time between state estimates, and $\mathbf{g} \in \mathbb{R}^3$ is the gravity vector. The symbol \otimes in (11) denotes the quaternion multiplication and $\mathbf{q}(\omega_{k-1} \Delta t)$ converts the Euler angles ω to quaternion representation. $\mathbf{f}_k \in \mathbb{R}^3$ and $\mathbf{w}_k \in \mathbb{R}^3$ are the linear acceleration and angular velocity measured by the IMU. \mathbf{q}_{k-1} is the orientation quaternion at time $k-1$, and $\mathbf{R}(\mathbf{q}_{k-1})$ is the corresponding rotation matrix that transforms vectors from the body (IMU) frame to the world (inertial) frame.

To robustly fuse sensor data with different update rates and to mitigate drift and noise—especially from inertial measurements—we use the *error-state* formulation of the EKF. Unlike the classical EKF, which directly estimates the full state, the ES-EKF maintains a nominal state and estimates a small additive error state. This approach improves numerical stability for orientation (notably for quaternions) and simplifies linearization by applying it only to the error dynamics rather than the full nonlinear model. The nominal state is propagated using the nonlinear model above, while the error state is handled using a linearized system with Gaussian noise. The following section details this process.

1) *Error State Model*: The error state represents small deviations from the nominal state:

$$\delta \mathbf{x}_k = \begin{bmatrix} \delta \mathbf{p}_k \\ \delta \mathbf{v}_k \\ \delta \theta_k \end{bmatrix} \in \mathbb{R}^9 \quad (12)$$

The error dynamics evolve as a linear time-varying system

$$\delta \mathbf{x}_k = \mathbf{F}_{k-1} \cdot \delta \mathbf{x}_{k-1} + \mathbf{L}_{k-1} \cdot \mathbf{n}_{k-1} \quad (13)$$

where $\mathbf{F}_{k-1} \in \mathbb{R}^{9 \times 9}$ is the state transition matrix of the error-state dynamics with respect to the error state itself, and $\mathbf{L}_{k-1} \in \mathbb{R}^{9 \times 6}$ is the noise mapping matrix that maps the IMU process noise into the error-state space, both evaluated at time step $k-1$.

$$\mathbf{F}_{k-1} = \begin{bmatrix} \mathbf{I}_3 & \Delta t \mathbf{I}_3 & \mathbf{0}_{3 \times 3} \\ \mathbf{0}_{3 \times 3} & \mathbf{I}_3 & -\mathbf{R}(\mathbf{q}_{k-1}) \cdot \mathbf{f}_{k-1} \times \Delta t \\ \mathbf{0}_{3 \times 3} & \mathbf{0}_{3 \times 3} & \mathbf{I}_3 \end{bmatrix}, \quad (14)$$

$$\mathbf{L}_{k-1} = \begin{bmatrix} \mathbf{0}_{3 \times 3} & \mathbf{0}_{3 \times 3} \\ \mathbf{I}_3 & \mathbf{0}_{3 \times 3} \\ \mathbf{0}_{3 \times 3} & \mathbf{I}_3 \end{bmatrix}, \quad (15)$$

and \mathbf{I}_3 represents a 3×3 identity matrix.

2) *Prediction Step Noise*: The prediction step is affected by noise $\mathbf{n}_k \sim \mathcal{N}(\mathbf{0}, \mathbf{Q}_k)$ where

$$\mathbf{Q}_k = \Delta t^2 \begin{bmatrix} \sigma_{\text{acc}}^2 & \mathbf{0}_{3 \times 3} \\ \mathbf{0}_{3 \times 3} & \sigma_{\text{gyr}}^2 \end{bmatrix} \quad (16)$$

where σ_{acc}^2 and σ_{gyr}^2 are the variances of the accelerometer and the gyroscope.

3) *Observation Noise*: The observation noise is modelled as $\mathbf{o}_k \sim \mathcal{N}(\mathbf{0}, \mathbf{R}_k)$ where $\mathbf{R}_k \in \mathbb{R}^{3 \times 3}$ is the measurement noise covariance matrix, representing the uncertainty in either the visual odometry or the CPP-based position measurement, depending on which observation is used at time step k . \mathbf{R}_k is used in the measurement update step of the Kalman filter. Specifically, it appears in the computation of the Kalman gain, where it quantifies the expected uncertainty in the incoming position measurement.

Based on the above modeling, we formulate the fusion algorithm shown in Algorithm 1, which integrates information from inertial, visual, and CPP-based positioning. Note that variables with a check mark ($\check{\cdot}$) denote predicted values from the motion model (prior estimates), while variables with a hat ($\hat{\cdot}$) represent corrected values after incorporating measurements (posterior estimates). The overall system architecture is shown in Fig. 13.

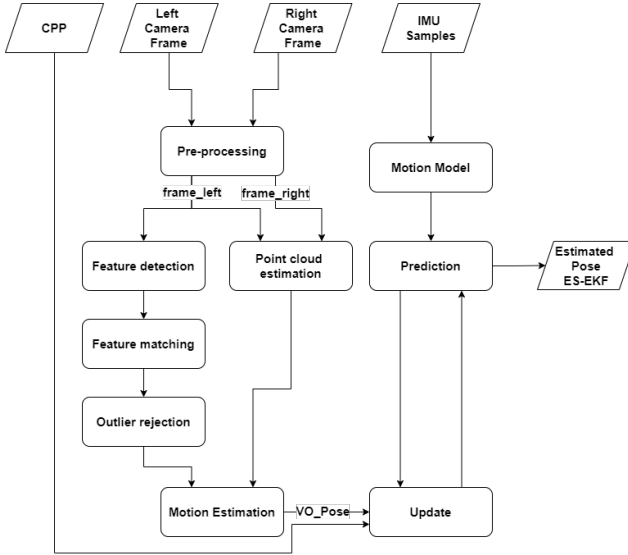


Fig. 13. Flow chart of the proposed VO and EKF system.

D. Scenario of fusion experiment

Let's consider a typical scenario where a vehicle is an agent whose motion is being estimated using an integrated CPP-based positioning system, stereo visual odometry, and inertial sensors. All individual source of sensor information have their own shortcomings. For example, the integrated CPP system is susceptible to the number of BSs available and LOS conditions during the estimation of the location. The application of the fusion should rectify this issue in NLOS conditions, and the inertial sensor would augment the visual odometry in estimating the trajectory.

Algorithm 1 ES-EKF based Fusion of VO, IMU and CPP Measurements

Require: Previous state $(\check{\mathbf{p}}_{k-1}, \check{\mathbf{v}}_{k-1}, \check{\mathbf{q}}_{k-1})$, covariance \mathbf{P}_{k-1} , IMU acceleration \mathbf{f}_{k-1} , angular velocity ω_{k-1} , process noise \mathbf{Q}_{k-1} , measurement noise covariance \mathbf{R}_k , measurement matrix \mathbf{H}_k , measurement $\mathbf{y}_k = \mathbf{H}_k \mathbf{x}_k + \mathbf{o}_k$ (if available, here \mathbf{y}_k is from either visual odometry or CPP)

Ensure: Updated state $(\hat{\mathbf{p}}_k, \hat{\mathbf{v}}_k, \hat{\mathbf{q}}_k)$ and covariance \mathbf{P}_k

- 1: **Predict state:**
- 2: $\check{\mathbf{p}}_k \leftarrow \check{\mathbf{p}}_{k-1} + \Delta t \check{\mathbf{v}}_{k-1} + \frac{1}{2} \Delta t^2 (\mathbf{R}(\check{\mathbf{q}}_{k-1}) \cdot \mathbf{f}_{k-1} + \mathbf{g})$ # Eq. (9)
- 3: $\check{\mathbf{v}}_k \leftarrow \check{\mathbf{v}}_{k-1} + \Delta t (\mathbf{f}_{k-1} + \mathbf{g})$ # Eq. (10)
- 4: $\check{\mathbf{q}}_k \leftarrow \check{\mathbf{q}}_{k-1} \otimes \mathbf{q}(\omega_{k-1} \Delta t)$ # Eq. (11)
- 5: **Propagate covariance:**
- 6: $\check{\mathbf{P}}_k \leftarrow \mathbf{F}_{k-1} \mathbf{P}_{k-1} \mathbf{F}_{k-1}^\top + \mathbf{L}_{k-1} \mathbf{Q}_{k-1} \mathbf{L}_{k-1}^\top$
- 7: **if** measurement \mathbf{y}_k is available **then**
- 8: **Compute Kalman gain:**
- 9: $\mathbf{K}_k \leftarrow \check{\mathbf{P}}_k \mathbf{H}_k^\top (\mathbf{H}_k \check{\mathbf{P}}_k \mathbf{H}_k^\top + \mathbf{R}_k)^{-1}$
- 10: **Estimate error state:**
- 11: $\delta \mathbf{x}_k \leftarrow \mathbf{K}_k (\mathbf{y}_k - h(\check{\mathbf{x}}_k))$, here $h(\check{\mathbf{x}}_k)$ is $\check{\mathbf{P}}_k$, assuming that the observation directly measures position.
- 12: **Correct predicted state:**
- 13: $\hat{\mathbf{p}}_k \leftarrow \check{\mathbf{p}}_k + \delta \mathbf{p}_k$
- 14: $\hat{\mathbf{v}}_k \leftarrow \check{\mathbf{v}}_k + \delta \mathbf{v}_k$
- 15: $\hat{\mathbf{q}}_k \leftarrow \check{\mathbf{q}}_k \otimes \mathbf{q}(\delta \theta_k)$
- 16: **Update covariance:**
- 17: $\mathbf{P}_k \leftarrow (\mathbf{I}_{9 \times 9} - \mathbf{K}_k \mathbf{H}_k) \check{\mathbf{P}}_k$
- 18: **else**
- 19: **No available measurement from either visual odometry or CPP:**
- 20: $(\hat{\mathbf{p}}_k, \hat{\mathbf{v}}_k, \hat{\mathbf{q}}_k, \mathbf{P}_k) \leftarrow (\check{\mathbf{p}}_k, \check{\mathbf{v}}_k, \check{\mathbf{q}}_k, \check{\mathbf{P}}_k)$
- 21: **end if**
- 22: **return** $(\hat{\mathbf{p}}_k, \hat{\mathbf{v}}_k, \hat{\mathbf{q}}_k, \mathbf{P}_k)$

For this scenario, we utilize the KITTI dataset [19]. Specifically, we use sequence 09 of the KITTI dataset to validate our proposed fusion system. The KITTI dataset provides recorded information on camera frames, IMU, and GPS data of a vehicle moving through an urban street. The GPS and IMU data is collected using OXTS sensor, which uses RTK to provide precise ground truth information on the trajectory. This is necessary to compare our computed trajectory with the ground truth trajectory. We simulate SRS and PRS-based trilateration with the LOS/NLOS data obtained from the simulation conducted using the methods described in Sec. IV-A. Fig. 14 visualizes the trajectory of sequence 09 using the ground truth information overlaid by the simulated LOS/NLOS paths for the same area in which sequence 09 is recorded.

Figure 15 compares the trajectory estimates from visual odometry and CPP using SRS and PRS signals. The CPP-based trajectories are shown only at locations where at least three BSs provide LOS conditions. Notably, when this condition is met, the CPP trajectory closely aligns with the ground truth, demonstrating the high positioning accuracy of the CPP method. To obtain a complete and consistent trajectory, we employ the proposed fusion system to integrate IMU and VO

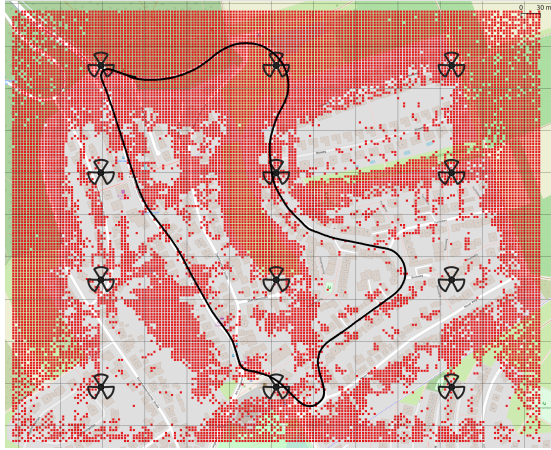


Fig. 14. Sequence 09 given by the black trajectory overlaid on the LOS/NLOS data obtained using simulation. In this figure, red squares indicate locations where at least three BSs maintain LOS conditions.

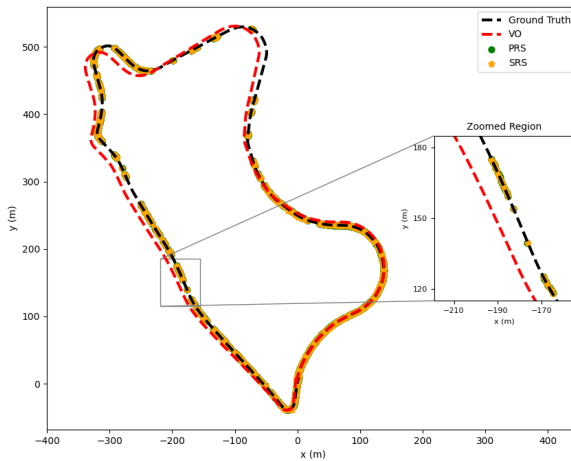


Fig. 15. Visual odometry, SRS, and PRS-based trajectory estimates on sequence 09. The zoomed region shows the inconsistent trajectory estimate by SRS and PRS due to the NLOS issue.

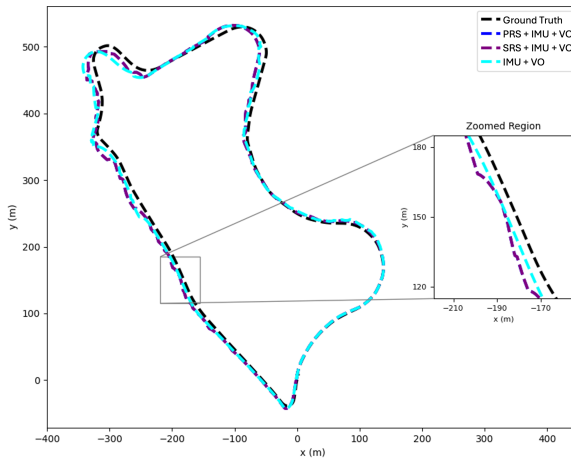


Fig. 16. Estimated trajectories using ES-EKF for both SRS and PRS based trajectory estimation.

data with CPP. The resulting trajectory is shown in Fig. 16.

Figure 16 presents a limited set of trajectory points to provide a visual overview of the estimated path; however, this is not sufficient for drawing definitive conclusions about the

system's performance. To quantitatively evaluate the accuracy of the estimated trajectories, we use the absolute trajectory error (ATE) and relative pose error (RPE) metrics, as defined in (17) and (18), respectively. ATE measures the square root of the average of the squared Euclidean distances between the estimated positions and the ground truth positions over all N timestamps or positions in the trajectory. P_k^{est} represents the estimated trajectory and P_k^{gt} represents the ground truth. Meanwhile, average RPE (translational) measures error in translation over a fixed interval Δ . P_t and $P_{t+\Delta}$ are pose estimates at time t and $t + \Delta$. Q_t and $Q_{t+\Delta}$ are corresponding poses in the ground truth trajectory. $(P_t P_{t+\Delta})_{trans}$ and $(Q_t Q_{t+\Delta})_{trans}$ are the translational component of the estimated and ground truth poses, respectively.

$$ATE = \sqrt{\sum_{k=1}^N \|P_k^{est} - P_k^{gt}\|^2} \quad (17)$$

$$RPE_{trans} = \frac{1}{N-\Delta} \sum_{t=1}^{N-\Delta} \| (Q_t^{-1} Q_{t+\Delta})_{trans} - (P_t^{-1} P_{t+\Delta})_{trans} \| \quad (18)$$

TABLE III
ABSOLUTE TRAJECTORY ERROR FROM ES-EKF

Sensors Fused	ATE (m)	RPE (deg)
VO	11.56	0.081
IMU + VO	15.60	0.068
SRS + IMU + VO	4.63	0.082
PRS + IMU + VO	4.66	0.081

From Table III, we can deduce that the integration of both SRS and PRS-based position estimates significantly improves the overall estimated error. Comparing our results with those from [48, Table 1], which meticulously collected data from other state-of-the-art systems, we find that our proposed solution achieves a marked improvement in ATE over all other state-of-the-art systems, by a factor of 2.

VIII. CONCLUSIONS

This paper presents a robust positioning system that leverages 5G infrastructure as a terrestrial alternative to traditional GNSS-based localization. Motivated by the challenges of operating in GNSS-denied scenarios, the proposed solution integrates Carrier Phase Positioning with machine learning-based LOS and NLOS wireless channel classification technique and multi-sensor fusion (using IMU and visual odometry data) into a unified, resilient positioning system.

We address key challenges in modern positioning systems, including carrier phase ambiguity resolution, measurement errors due to multipath effects, and positioning continuity during LOS outages. Our multifrequency-based phase averaging approach enables single-epoch range estimation, simplifying system architecture while maintaining centimeter-level accuracy in LOS condition. Furthermore, we propose a deep learning framework for real-time LOS/NLOS classification using SRS-derived channel impulse responses, which significantly improves positioning robustness by classifying and discarding corrupted NLOS signals. The integration of visual odometry

and inertial data with cellular sounding reference signal within an Error-State Extended Kalman Filter enables seamless trajectory tracking, even under conditions where a single positioning measurement or technology becomes degraded or unavailable.

Through extensive simulations based on 3GPP-compliant channel models and real-world evaluation using the KITTI dataset, we demonstrate that our system achieves high positioning accuracy and continuity across varied scenarios. Experimental results confirm the system's effectiveness in maintaining localization with absolute trajectory errors below 5 meters, even in environments with significant signal obstructions. Overall, this study validates the feasibility of using 5G networks as a resilient, scalable, and high-accuracy positioning platform, offering a promising path forward for mission-critical applications. Future work will focus on real-world deployments, optimization of BS placement for urban and indoor scenarios, and the extension of CPP methods to support high-mobility users.

REFERENCES

- [1] E. Ghizzo *et al.*, "Assessing jamming and spoofing impacts on GNSS receivers: Automatic gain control (AGC)," *Signal Processing*, vol. 228, p. 109762, 2025.
- [2] D. Borio *et al.*, "Impact and detection of GNSS jammers on consumer grade satellite navigation receivers," *Proc. IEEE*, vol. 104, no. 6, pp. 1233–1245, 2016.
- [3] M. Spanghero *et al.*, "GNSS jammer localization and identification with airborne commercial GNSS receivers," *IEEE Trans. Inf. Forensics Secur.*, 2025.
- [4] L. Chen *et al.*, "Carrier phase ranging for indoor positioning with 5G NR signals," *IEEE Internet Things J.*, vol. 9, no. 13, pp. 10908–10919, 2021.
- [5] Q. Liu *et al.*, "Simulation and analysis of device positioning in 5G ultra-dense network," in *IWCNC*, 2019, pp. 1529–1533.
- [6] R. M. Ferre *et al.*, "Positioning reference signal design for positioning via 5G," in *Finnish URSI Convention on Radio Science*. URSI, 2019.
- [7] M. Koivisto *et al.*, "Joint device positioning and clock synchronization in 5G ultra-dense networks," *IEEE Trans. Wireless Commun.*, vol. 16, no. 5, pp. 2866–2881, 2017.
- [8] P. Gertzell *et al.*, "5G multi-BS positioning with a single-antenna receiver," in *IEEE PIMRC*, 2020, pp. 1–5.
- [9] H. Kim *et al.*, "Cooperative localization with constraint satisfaction problem in 5G vehicular networks," *Trans. Intell. Transp. Syst.*, vol. 23, no. 4, pp. 3180–3189, 2022.
- [10] M. Malmström *et al.*, "5G positioning-a machine learning approach," in *16th Workshop on Positioning, Navigation and Communications (WPNC)*. IEEE, 2019, pp. 1–6.
- [11] M. M. Butt *et al.*, "RF fingerprinting and deep learning assisted ue positioning in 5G," in *IEEE VTC-Spring*, 2020, pp. 1–7.
- [12] J. Gante *et al.*, "Deep learning architectures for accurate millimeter wave positioning in 5G," *Neural Processing Letters*, vol. 51, no. 1, pp. 487–514, 2020.
- [13] P. Stephan *et al.*, "Angle-delay profile-based and timestamp-aided dissimilarity metrics for channel charting," *IEEE Transactions on Communications*, 2024.
- [14] A. Fouda *et al.*, "Toward cm-level accuracy: Carrier phase positioning for IIoT in 5G-advanced NR networks," in *IEEE PIMRC*, 2022, pp. 782–787.
- [15] Y. Wang *et al.*, "Recent progress on 3GPP 5G positioning," in *IEEE VTC-Spring*. IEEE, 2023, pp. 1–6.
- [16] H.-S. Cha *et al.*, "5G NR positioning enhancements in 3GPP Release-18," *IEEE Commun. Stds. Mag.*, vol. 9, no. 1, pp. 22–27, 2025.
- [17] L. Italiano *et al.*, "A tutorial on 5G positioning," *IEEE Commun. Surveys Tuts.*, pp. 1–1, 2024.
- [18] S. Fan *et al.*, "Carrier phase-based synchronization and high-accuracy positioning in 5G new radio cellular networks," *IEEE Trans. Commun.*, vol. 70, no. 1, pp. 564–577, 2021.
- [19] A. Geiger *et al.*, "Vision meets robotics: The KITTI dataset," *Int. J. Rob. Res.*, vol. 32, no. 11, p. 1231–1237, Sep. 2013. [Online]. Available: <https://doi.org/10.1177/0278364913491297>
- [20] J. Hoydis *et al.*, "Sionna RT: Differentiable ray tracing for radio propagation modeling," in *IEEE GC Wkshps*. IEEE, 2023, pp. 317–321.
- [21] 3GPP TR 38.859, "Study on expanded and improved NR positioning," June 2024.
- [22] J. Ou *et al.*, "Single-shot carrier phase positioning method with wrapping effect solution in 5G new radio cellular networks," in *IEEE GLOBECOM*, 2024, pp. 313–318.
- [23] Z. Deng and Z. Ma, "A low complexity localization method based on 5G carrier phase," in *9th Intl. Conf. on Intelligent Computing and Signal Processing (ICSP)*, 2024, pp. 872–877.
- [24] M. Abuyaghji *et al.*, "Positioning in 5G networks: Emerging techniques, use cases, and challenges," *IEEE Internet Things J.*, vol. 12, no. 2, pp. 1408–1427, 2025.
- [25] H. Wymeersch *et al.*, "Fundamental performance bounds for carrier phase positioning in cellular networks," in *IEEE GLOBECOM*, 2023, pp. 7478–7483.
- [26] Y. Gao *et al.*, "Improving non-line-of-sight identification in cellular positioning systems using a deep autoencoding and generative adversarial network model," *Sensors*, vol. 24, no. 1919, p. 6494, Jan. 2024.
- [27] P. A. N. Jayawardana *et al.*, "Machine-learning-based LOS detection for 5G signals with applications in airport environments," *Sensors*, vol. 23, no. 3, p. 1470, 2023.
- [28] H. Talebian *et al.*, "An ensemble ML model design to classify LOS/NLOS in 5G-NR InF propagation environment."
- [29] L. Fluerautor *et al.*, "Self-learning detection and mitigation of non-line-of-sight measurements in ultra-wideband localization," in *IEEE IPIN*. IEEE, 2021, pp. 1–8.
- [30] T. Qin *et al.*, "VINS-Mono: A robust and versatile monocular visual-inertial state estimator," *IEEE Transactions on Robotics*, vol. 34, no. 4, pp. 1004–1020, 2018.
- [31] E. Hong and J. Lim, "Visual inertial odometry using coupled nonlinear optimization," in *2017 IEEE/RSJ International Conference on Intelligent Robots and Systems (IROS)*, 2017, pp. 6879–6885.
- [32] A. I. Mourikis and S. I. Roumeliotis, "A multi-state constraint kalman filter for vision-aided inertial navigation," in *Proceedings 2007 IEEE International Conference on Robotics and Automation*, 2007, pp. 3565–3572.
- [33] D. Scaramuzza and Z. Zhang, "Visual-inertial odometry of aerial robots," 2019. [Online]. Available: <https://arxiv.org/abs/1906.03289>
- [34] Y. Pan *et al.*, "Adaptive VIO: Deep visual-inertial odometry with online continual learning," 2024. [Online]. Available: <https://arxiv.org/abs/2405.16754>
- [35] G. Delama *et al.*, "UVIO: An UWB-aided visual-inertial odometry framework with bias-compensated anchors initialization," 2023. [Online]. Available: <https://arxiv.org/abs/2308.00513>
- [36] M. Giordani *et al.*, "Toward 6G networks: Use cases and technologies," *IEEE Commun. Mag.*, vol. 58, no. 3, pp. 55–61, 2020.
- [37] H. Wymeersch *et al.*, "6G radio requirements to support integrated communication, localization, and sensing," in *EuCNC/6G Summit*. IEEE, 2022, pp. 463–469.
- [38] J. A. del Peral-Rosado *et al.*, "Survey of cellular mobile radio localization methods: From 1G to 5G," *IEEE Commun. Surveys Tuts.*, vol. 20, no. 2, pp. 1124–1148, 2017.
- [39] 3GPP TS 38.305, "5G; NG Radio Access Network (NG-RAN); Stage 2 functional specification of User Equipment (UE) positioning in NG-RAN," 2024, v18.3.0, Release 18.
- [40] 3GPP TS 38.214, "5G; NR; physical layer procedures for data," Dec. 2024, v18.4.0, Release 18.
- [41] 3GPP TS 38.211, "5G; NR; physical channels and modulation," Dec. 2024, release 18.
- [42] 3GPP TR 21.918, "Release 18 description; summary of Rel-18 work items," Mar. 2024.
- [43] 3GPP TR 38.901, "Study on channel model for frequencies from 0.5 to 100 GHz," Mar. 2022.
- [44] X. Li, "GNSS repeater based differential indoor positioning with multi-epoch measurements," *IEEE Transactions on Intelligent Vehicles*, vol. 8, no. 1, pp. 1–813, oct 2021.
- [45] 3GPP Tdoc R1-1901980, "Further discussion of NR RAT-dependent DL positioning," Mar. 2019.
- [46] J. Nikonowicz *et al.*, "Indoor positioning in 5G-advanced: Challenges and solution toward centimeter-level accuracy with carrier phase enhancements," *IEEE Wireless Commun.*, vol. 31, no. 4, pp. 268–275, 2024.
- [47] 3GPP Tdoc R1-2306873, "Remaining issues on NR DL and UL carrier phase positioning," August 2023.
- [48] H. Zhan *et al.*, "DF-VO: What should be learnt for visual odometry?" 2021. [Online]. Available: <https://arxiv.org/abs/2103.00933>